mater.scichina.com link.springer.com

Published online 18 September 2023 | https://doi.org/10.1007/s40843-023-2561-8
Sci China Mater 2023, 66(10): 3968–3976

Selective epitaxial growth of organic heterostructure *via* cocrystal engineering: Towards oriented signal conversion

Qiang Lv[1,2], Xue-Dong Wang[1*], Yue Yu[1], Yan-Jun Yu[1], Min Zheng[2*] and Liang-Sheng Liao[1,3*]

ABSTRACT **The integration of multiple components with different functionalities into a hierarchical organic nanosystem (HON) has attracted significant attention in optoelectronic applications. However, the rational construction of HONs with ultra-low lattice mismatch (η) remains a major challenge due to the inherent structural incompatibility of different materials. Cocrystal engineering holds great promise as a powerful means to explore the controllable fabrication of HONs, but a systematic demonstration has yet to be achieved. Here, we present a cocrystal engineering strategy for ultra-low lattice mismatch heteroepitaxy of HONs, which exhibits sufficient versatility for integrating a variety of materials to construct HONs. Through experimental synthesis, we have realized a series of representative HONs, including three-segment (η_1 = 0.7%), branched (η_2 = 0.8%), and core/shell (η_3 = 0.6%) nanostructures, with lattice mismatch rates significantly lower than those previously reported for HONs (5%–10%). Furthermore, we selectively synthesized substructures of core/shell, including three-segment and sandwich-like nanowires, revealing the role of interface engineering in the formation of unique HONs. As a conceptual validation, the fabricated HONs have successfully achieved oriented photon signal conversion, laying a solid material foundation for constructing the next generation of integrated optoelectronic devices.**

Keywords: organic heterostructures, epitaxy, lattice mismatch, cocrystal, integrated photonics

INTRODUCTION

Complex heterostructured materials with more than two components can effectively combine the advantages and overcome the weaknesses of the individual components [1,2]. Thus, heterostructure materials have exhibited potential advantages in many applications such as catalysis [3], plasmonics [4], electronics [5], optoelectronics [6], and so on [7]. It is worth noting that the characteristics and functions of heterostructures significantly depend on their spatial orientation and interfaces [8]. Therefore, the controlled preparation of heterostructure with different spatial orientations and architectures is an important theme for the development of novel functional heterostructures. Until now, various inorganic heterostructures with well-defined compositions, morphologies, and functionalities have been developed [3,9–11]. For example, eight CdS nanocrystals are hierarchically grown onto the central region of CdSe nanorods to form octopod-shaped nanocrystals *via* a cation exchange method [12].

Compared with inorganic components, organic semiconductor molecules exhibit obvious advantages for optoelectronics applications [13–19] benefiting from their large optical cross-sections [20], tunable structures [21], broad wavelength tunability [22], and low-cost solution processing [23]. Currently, lots of efforts have been devoted to synthesizing organic heterostructures with different architectures including the core/shell [24,25], branch [26,27], triblock [28,29], dumbbell-like [30], lateral type [31], and so on [32]. Among approaches for synthesizing organic heterostructures, the epitaxial growth method stands out as a powerful tool [33–35]. However, owing to the difficulty in solving the lattice mismatch of distinct materials, it remains a great challenge to rationally construct hierarchical organic nanosystems (HONs) in ultralow lattice-mismatch heteroepitaxy, which is crucial for the performance of final devices [36]. In particular, the previously reported organic heterostructures are implemented on different molecular systems, which makes it more difficult to overcome the incompatible problem of systems to achieve the interconnection of building blocks for integrated optoelectronics. Notably, cocrystals formed by two or more molecules crystallized together in a single lattice driven by intermolecular non-covalent interactions, which could provide an important platform for exploring these challenges of HONs, but have so far not been systematically demonstrated.

In this work, we demonstrate a strategy of cocrystal engineering for ultralow lattice-mismatch heteroepitaxy of HONs, which is sufficiently versatile to enable the integration of multiple materials. During the hierarchical self-assembly process, the similar crystal packing and compatibilities of organic cocrystals feasibly enable the low lattice mismatch rate (η), thus avoiding the occurrence of phase separation and homogeneous nucleation. We prepared four types of benzo[ghi]perylene (BGP)-based cocrystals, and then experimentally synthesized a serial of typical HONs including triblock (η_1 = 0.7%), branch (η_2

[1] Institute of Functional Nano & Soft Materials (FUNSOM), Jiangsu Key Laboratory for Carbon-Based Functional Materials & Devices, Soochow University, Suzhou 215123, China
[2] National Engineering Laboratory for Modern Silk, College of Textile and Clothing Engineering, Research Center of Cooperative Innovation for Functional Organic/Polymer Material Micro/Nanofabrication, Soochow University, Suzhou 215123, China
[3] Macao Institute of Materials Science and Engineering, Macau University of Science and Technology, Taipa 999078, Macao SAR, China
* Corresponding authors (emails: wangxuedong@suda.edu.cn (Wang XD); zhengmin@suda.edu.cn (Zheng M); lsliao@suda.edu.cn (Liao LS))

= 0.8%), and core/shell (η_3 = 0.6%) nanostructures, whose lattice mismatch rates are considerably lower than those of previously reported HONs without diversity (5%–10%). Moreover, we selectively synthesize the substructures of core/shell HONs including triblock and sandwich-like nanowires *via* the thermodynamically favored route by adjusting the reaction temperature, thus revealing the role of interfacial energies in modulating the formation of distinctive HONs. As a proof-of-concept application, these obtained HONs demonstrate different photon guidance and manipulation as photonic device prototypes such as optical signal converters with multi-color/channel characteristics in different orientations. This strategy provides a new window for the ultralow lattice-mismatch heteroepitaxy of virtually any hierarchical nanostructures.

RESULTS AND DISCUSSION

Ultralow lattice-mismatch heteroepitaxy strategy

As shown in Fig. 1a, we schematically represent a strategy of cocrystal engineering for ultralow lattice-mismatch heteroepitaxy of hierarchical organic nanostructures. Due to the difference in the strength of the intermolecular non-covalent interactions and the solubility of the molecules, the cocrystal 1 with strong charge-transfer (CT) interaction first nucleates and grows, becoming the crystalline substrate for the heterostructure. Then, cocrystal 2 epitaxially grows along the exposed face of cocrystal 1 to form a heterostructure structure. During the hierarchical self-assembly process of multi-component, cocrystal engineering based on the same donor can effectively avoid the problem of incompatibilities of different acceptors, thus realizing

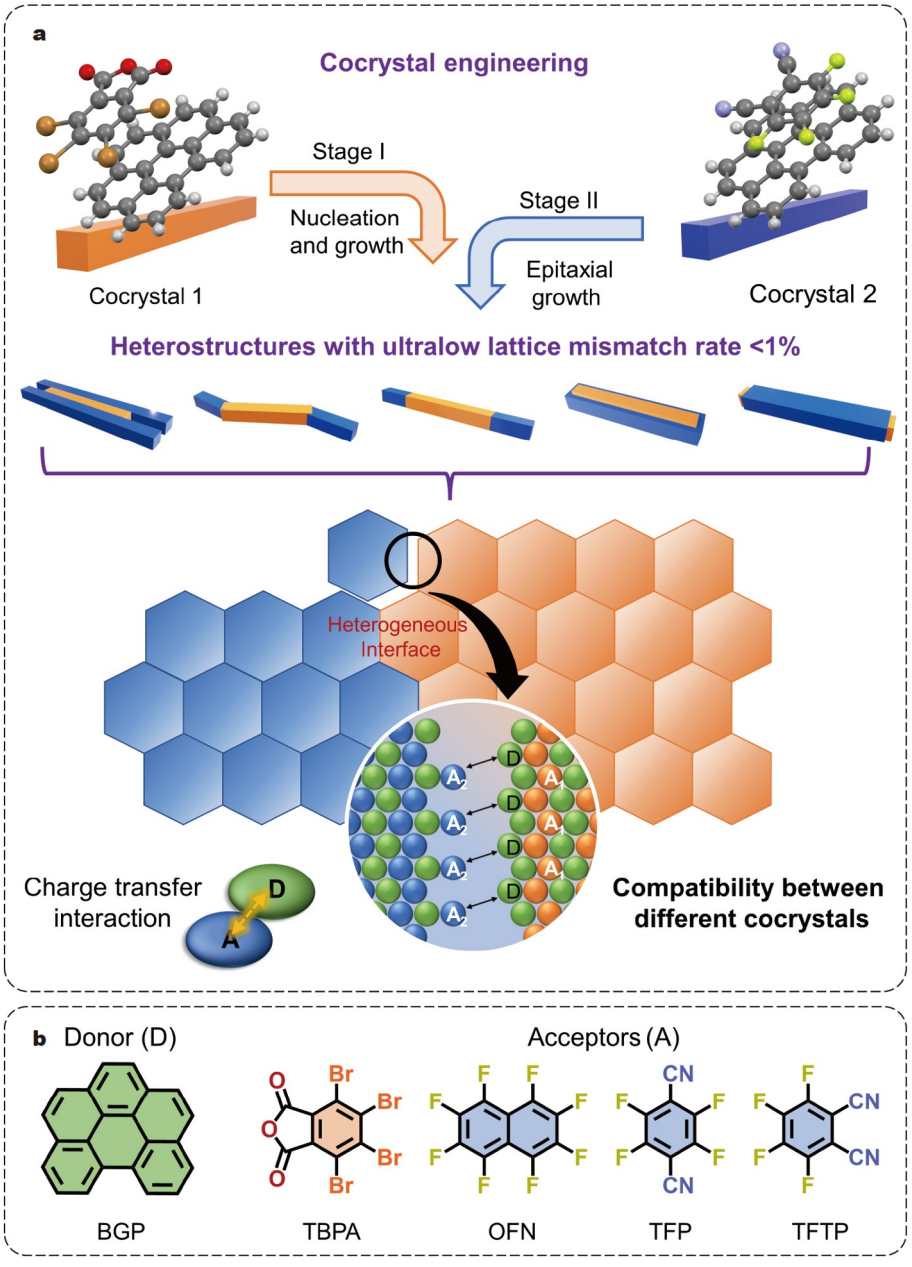

Figure 1 Epitaxial growth of hierarchical organic heterostructures based on cocrystal engineering. (a) Schematic illustration of the cocrystal engineering strategy for ultralow lattice-mismatch heteroepitaxy of HONs. (b) Molecular structures of the donor and acceptors for cocrystal engineering.

the heterogeneous interface with an ultralow lattice mismatch rate. In detail, we experimentally prepared four types of organic cocrystal including BGP-tetrabromophthalicanhydride (TBPA), BGP-octafluoronaphthalene (OFN), BGP-tetrafluoro-terephthalonitrile (TFP), BGP-tetrafluorophthalonitrile (TFTP) through a solution self-assembly method (Fig. 1b). Among them, the BGP-TBPA cocrystals were selected as crystalline substrates for epitaxial growth of other organic crystals, due to the strong CT interaction and low solubility of TBPA molecules leading to the first nucleation and growth. Scanning electron microscopy (SEM) images show the one-dimensional (1D) morphology of BGP-TBPA cocrystal with a length of 20–60 μm and a diameter of 2–4 μm (Fig. S1). The fluorescence microscopy (FM) shows that the BGP-TBPA emission color is orange under ultraviolet (UV) excitation (Fig. S1). Furthermore, the average sizes, luminescence lifetimes, and PL quantum yields of these organic crystals are shown in Figs S2–S4 and Table S1. Notably, the BGP-TBPA single crystal with inherent anisotropy features, displays two basal (002) planes, four ends (101) planes, and four edges (011) planes *via* the simulation of a single crystal (Fig. S5). At the same time, the prerequisites of epitaxial growth are the small lattice mismatch between two or more crystals, that is, the minimization of the interfacial energy of the heterojunction in organic heterostructures [37]. Owing to the difference in the topological structures and lattice parameters (Tables S2–S6, Figs S5–S9), the other cocrystals can only epitaxially grow on the selective surfaces with a matched lattice of the BGP-TBPA cocrystals to achieve the interfacial energy balance in the heterojunction, leading to the formation of oriented hierarchical heterostructures. At the same time, the stronger CT interactions result in the BGP-TBPA cocrystal undergoing a primary self-assembly process as a preformed seed nanowire in the first stage of the epitaxial growth process (Table S7). These heterostructures with ultralow lattice mismatch, including blocks, branches, and core shells, are discussed in detail below. Moreover, the photoluminescence (PL) spectra of these cocrystals display a good overlap with the absorption spectra of the BGP-TBPA substrate (Fig. S10), indicating that these heterostructure microwires composed of different cocrystals can be applied in integrated photonics such as active waveguide, signal converts, and logic gate [38,39].

Horizontal epitaxial growth

The scheme for the synthesis of branch heterostructure is shown in Fig. 2a, in which the preformed BGP-TBPA cocrystals are used as seeds for the epitaxial growth of BGP-OFN microwires. Owing to the anisotropic structure of BGP-TBPA, the secondary BGP-OFN can only epitaxially grow on the selective surface (002) of the BGP-TBPA seeds with smaller lattice mismatch to form the branch heterostructures with lateral orientations. In addition, the number of BGP-OFN branches on the backbone can be regulated by tuning the stoichiometric ratio of multi-components (see detailed experiment method in Supplementary information). To deeply understand the epitaxial growth process of the branch heterostructures, we recorded the video data by tracking the real-time growth processes of BGP-OFN cocrystals on the BGP-TBPA cocrystals. As shown in Fig. $2b_1$–b_6, the bright field images of branch microwires are captured, which is marked with the formation times of the branch from 0–125 s. At the early stage, the BGP-TBPA microwire as the trunk part first nucleates from the mixed solution and elongates to tens of micrometers (Fig. $2b_1$). Then, the BGP-OFN microwire starts to nucleate heterogeneously on the side planes of the BGP-TBPA microwire and eventually grows to tens of micrometers (Fig. $2b_2$–$2b_6$). Fig. $2b_7$ demonstrates the FM image of the obtained branch heterostructure excited by unfocused UV light (330–380 nm). The trunk microwire exhibits orange light-emitting, while the branches emit blue light. In addition, Fig. 2c, d demonstrate typical FM image of obtained heterostructures. It can be seen that single-branch or double-branch microwires with a length of 60–70 μm were successfully prepared. SEM characterization clearly shows the architecture of the as-prepared branch heterostructure, where the BGP-OFN microwire laterally grows on BGP-TBPA (Fig. 2e and Fig. S11). The corresponding energy-dispersive X-ray spectroscopy (EDS) elemental mapping displays that the Br element is distributed in the middle area, whereas F distributes on both sides of the nanostructure, indicating the successful growth of BGP-OFN microwire on basal facets of seed BGP-TBPA (Fig. 2f, g). Transmission electron microscope (TEM) image of an individual heterostructure clearly shows the interface of branch and trunk microwire, further confirming the horizontal growth of BGP-OFN on the BGP-TBPA trunk (Fig. 2h). Importantly, the selected area electron diffraction (SAED) pattern taken at the branch and trunk piece of the heterostructure shows the diffraction spots clearly, which can be ascribed to the (020) and (200) planes of BGP-TBPA and the (200) planes of BGP-OFN (Fig. 2i, j), confirming the epitaxial growth of BGP-OFN microwires along an axis of BGP-TBPA. The crystal structure of BGP-OFN and BGP-TBPA microwires was verified by single crystal X-ray diffraction (XRD) analysis. Owing to the difference in topological structures, BGP-TBPA and BGP-OFN possess different crystal parameters (Tables S2 and S3). Interestingly, the interplanar spacing (002) of BGP-TBPA is almost two times that of the parameter (020) of BGP-OFN (Fig. 2k). It can be deduced that the epitaxial relationship between BGP-TBPA and BGP-OFN is $(002)_{BGP\text{-}TBPA}||(020)_{BGP\text{-}OFN}$. Therefore, it is possible to selectively grow BGP-OFN along *a* axis of BGP-TBPA, due to the smaller lattice mismatch ($\eta_1 = 0.7\%$). As expected, BGP-OFN crystals selectively grew on the side surface of the trunk but not on the entire surface to form branch heterostructures (Fig. 2e, h). Furthermore, XRD was also used to confirm the crystal structure of the branch heterostructure, clearly showing the diffraction peaks of BGP-TBPA and BGP-OFN cocrystal (Fig. S12). In addition, the PL of an individual branch microwire at different micro areas was characterized by the laser scanning confocal microscope equipped with a 375-nm laser. As shown in Fig. S13b, the emission from location 1 (marked in Fig. S13a) is in good consistence with that of BGP-OFN, and the orange-emitting from location 2 corresponding to the BGP-TBPA emission, and the emission at junction including both emissions of two cocrystals, which suggests that the entire branch microwire are made up of BGP-OFN and BGP-TBPA microwires. In general, the growth mechanism can be concluded that the (020) panels of BGP-OFN well match with (002) planes of BGP-TBPA crystals, and grow along *a* axis of BGP-TBPA to achieve the interfacial energy balance.

Longitudinal epitaxial growth

Fig. 3a presents the scheme for the synthesis of triblock heterostructures, in which the BGP-TBPA provides the sites for the heterogeneous nucleation and epitaxial growth of BGP-TFP. In

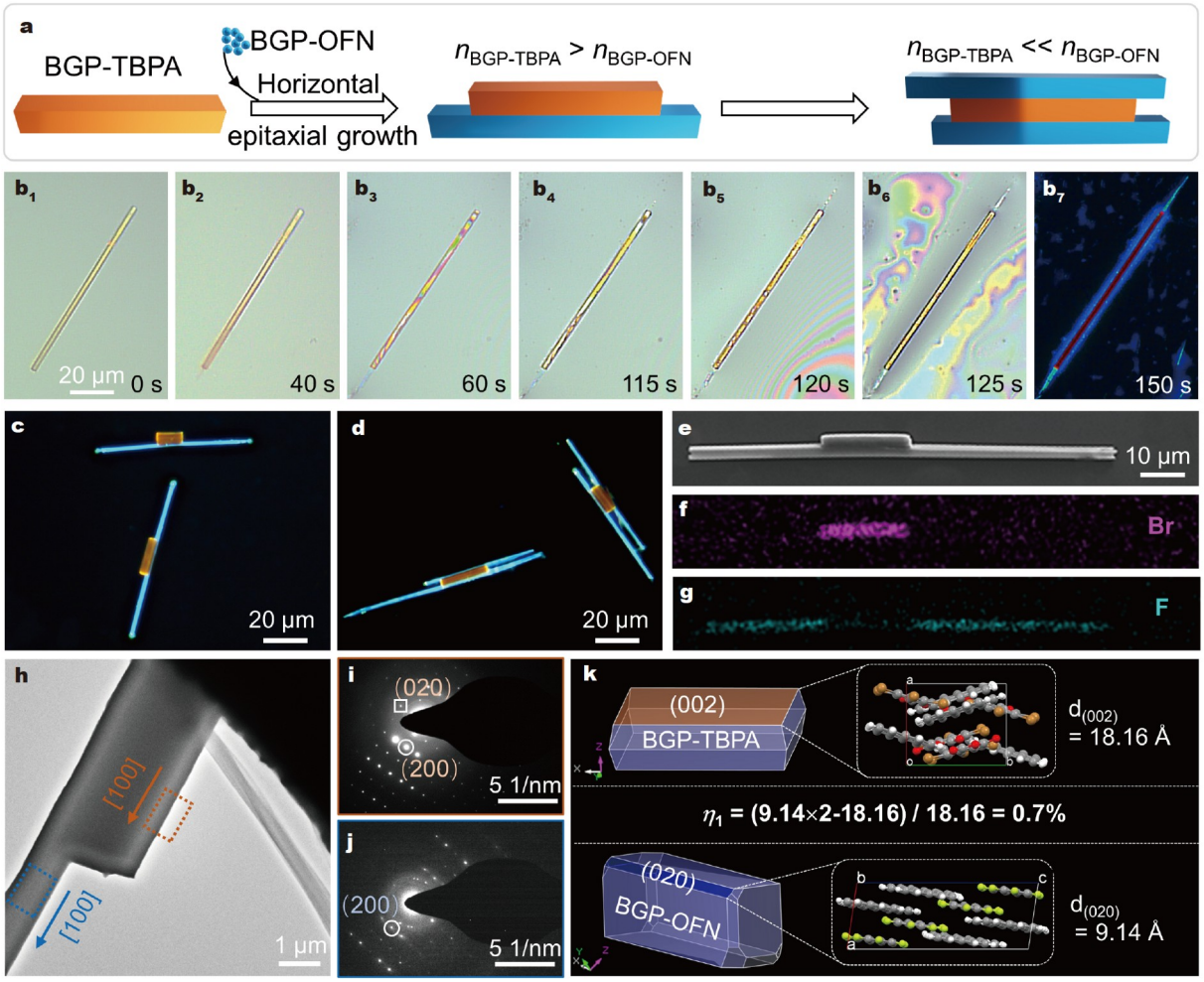

Figure 2 Analysis of branch heterostructure microwires. (a) Horizontal epitaxial growth of the branch heterostructure by the BGP-OFN microwire on the BGP-TBPA microwire. (b_1–b_7) The evolution processes of branch heterostructures at different time intervals are recorded by the corresponding real-time video. All scale bars are 20 μm. (c, d) FM images of branch heterostructures with single or double branches. (e) SEM image of a typical branch microwire, and the corresponding EDS elemental mapping for (f) Br and (g) F; scale bar: 10 μm. (h) TEM image of a typical branch microwire, and the corresponding SAED patterns of the branch microwire at (i) trunk and (j) branch positions. (k) Predicted growth morphology of BGP-TBPA and BGP-OFN cocrystals, and the corresponding lattice mismatching ratio (η_1) of the branch heterostructure.

addition, the distribution of the BGP-TFP microwire can be regulated from one tip to two tips of the substrate by adjusting the stoichiometric ratio of molecules during the co-assembly process (see detailed synthesis method in Supplementary information). As shown in Fig. 3b, c, block and triblock microwires have been successfully prepared. It can be seen that the BGP-TFP microwire only grows on the terminal facets of BGP-TBPA along its longitudinal direction. As shown in Fig. 3d, the selective growth of BGP-TFP microwires on the end planes of BGP-TBPA can be observed clearly in the SEM image. At the same time, the SEM images of triblock microwires in different growth indicate that the BGP-TFP cocrystal nucleates heterogeneously on the end planes of the BGP-TBPA cocrystal, and then grows to tens of micrometer (Figs S11, S14). The corresponding EDS elemental mapping demonstrates that the F element is distributed on both sides of the triblock microwire, whereas Br is confined in the central area, indicating the successful growth of the BGP-TFP microwire on both terminal facets of BGP-TBPA (Fig. 3e, f). In addition, the XRD patterns of triblock microwires demonstrate that the characteristic diffraction peaks of the BGP-TFP and BGP-TBPA exist simultaneously (Fig. S15), indicating the successful synthesis of the desired triblock heterostructures. At the same time, the spatially resolved PL spectrum of the primary triblock microfilament further confirms that it is composed of BGP-TFP and BGP-TBPA cocrystals (Fig. S13c, d). The TEM image of a typical heterostructure clearly shows the longitudinal growth of BGP-TFP on the one of end facets of BGP-TBPA microwires (Fig. 3g). The corresponding SAED pattern taken at two segments of the heterostructure shows the diffraction spots clearly, which can be ascribed to the (020) plane of BGP-TFP and (010) and (200) planes of BGP-TBPA (Fig. 3h, i), and demonstrates the oriented growth of BGP-TFP along the *b* axis, and the growth of BGP-TBPA along *a* axis. It is worth noting that the BGP-TFP crystals selectively grew along the major axis of the BGP-TBPA but not on the entire end surface to form Z-like triblock microwires with centrosymmetric (Fig. S14). This facet-selective growth originates from the smaller lattice mismatch between the terminal planes of the two crystals. Furthermore, the crystal structure of BGP-TFP microwires was verified by single crystal XRD analysis, and the

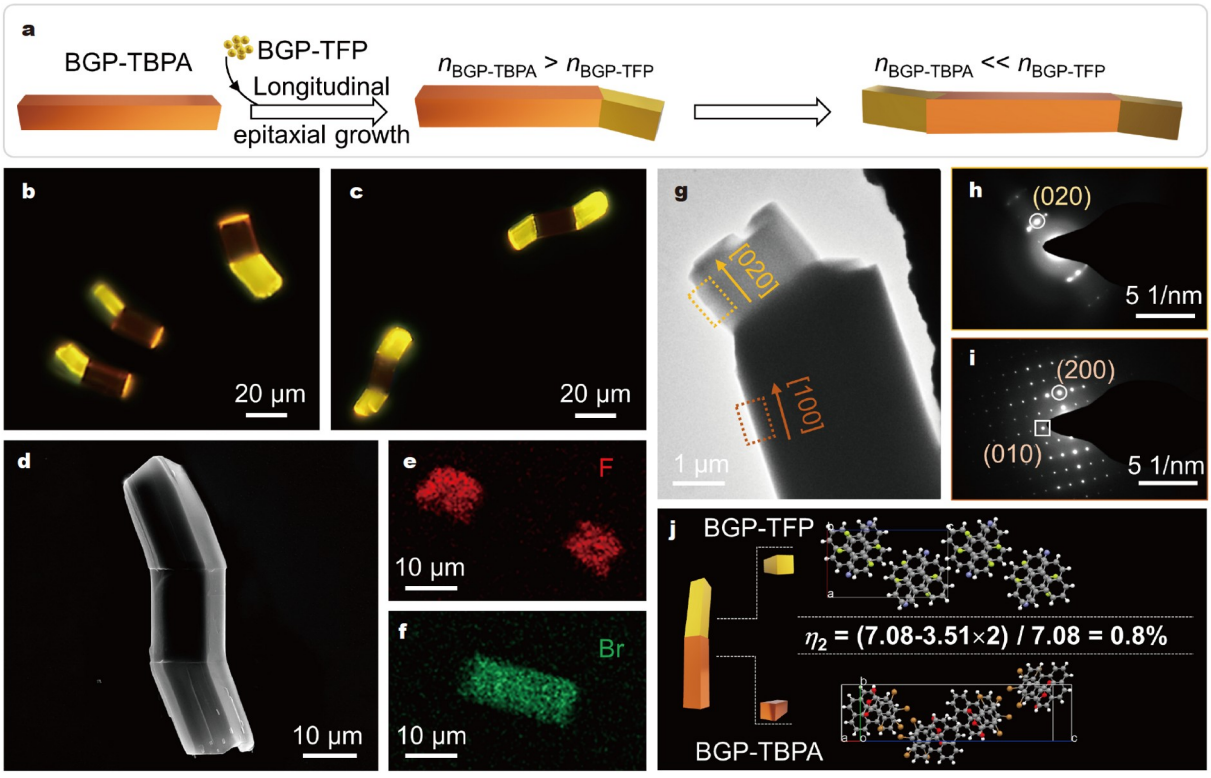

Figure 3 Characterization of organic triblock heterostructure microwires. (a) Longitudinal epitaxial growth of the triblock heterostructure by the BGP-TFP microwire on the BGP-TBPA microwire. (b, c) FM images of diblock and triblock microwires. (d) SEM image of a typical triblock microwire. EDS elemental mappings for (e) F and (f) Br. (g) TEM image of a typical triblock microwire, and the corresponding SAED patterns of triblock microwires at (h) tip and (i) central positions. (j) Molecular arrangements of the BGP-TFP (020) crystal plane and BGP-TBPA (101) crystal plane, and the corresponding lattice mismatching ratio (η_2) of triblock microwire at the junction.

simulated data show that the (020) planes of BGP-TFP match well with (101) planes of BGP-TBPA (Fig. 3j). It can be deduced that the epitaxial relationship between BGP-TFP and BGP-TBPA is $(020)_{BGP-TFP}||(101)_{BGP-TBPA}$. A lower lattice mismatch is more favorable for the epitaxial growth of organic heterostructures as it minimizes the interfacial energy of the heterogeneous structure between the two different crystal planes. Therefore, it is possible to selectively grow BGP-TFP along the major axis of BGP-TBPA, due to the smaller lattice mismatch (η_2 = 0.8%). So, the growth mechanism of the heterostructure can be concluded, in which the (020) panels of BGP-TFP well match with (101) planes of BGP-TBPA crystals, and grow along the major axis to form a Z-like triblock microwire with centrosymmetric.

Longitudinal and horizontal epitaxial growth

As mentioned above, different oriented hierarchical organic microwires including the horizontal and longitudinal directions have been successfully prepared by varying the secondary crystals. In addition to changing the structures of the crystal, carefully turning the reaction conditions is another way to prepare oriented hierarchical microwires. Based on the entropy-driven mechanism of crystal growth, the crystal facets with strong attachment energies grow more rapidly and hence grow out and cannot be observed, that is, high surface energy facets are eliminated, resulting in the aggregation of nanoparticles into a crystal. As shown in Table S2, the simulated data of the BGP-TBPA crystal show that the crystal facets with higher attachment energies generally form a small area, due to the deposition of many nanoparticles. Given good lattice matching between BGP-TFTP and BGP-TBPA, the attachment energies of different crystal planes of BGP-TBPA can drive the formation of differently oriented heterostructure microwires during the epitaxial growth process of BGP-TFTP cocrystal. As presented in Fig. 4a, BGP-TBPA microwires chosen as crystalline substrates, BGP-TFTP microwires selectively epitaxially grow on their end, edge, and basal facets *via* the thermodynamically favored route by adjusting the reaction temperature to form primary triblock, sandwich, and core/shell heterostructures, respectively. The evolution of core/shell heterostructures at different reaction stages is presented in Fig. $4b_1$–Fig. $4b_6$, which shows the selective growth behavior of BGP-TFTP on seed BGP-TBPA during the co-assembly process. Notably, the BGP-TFTP microwire first forms sticks at the terminals of the seed microwires along the longitudinal axis, and then epitaxially grows on the side along the horizontal axis, owing to the higher surface energy of the tip facets relative to the feasible compared with side-selective growth (Fig. S16).

Finally, BGP-TFTP completely covers BGP-TBPA forming a core/shell microwire. The aforementioned result demonstrates that the selective growth of BGP-TFTP not only lattice matches well with BGP-TBPA but also depends on the surface-interface energy balance of the crystal plane. The FM images in Fig. 4c, d show that the BGP-TFTP microwires selectively epitaxial grow on different facets of seed BGP-TBPA to form the sandwich and core/shell heterostructure microwires. Notably, the TEM image

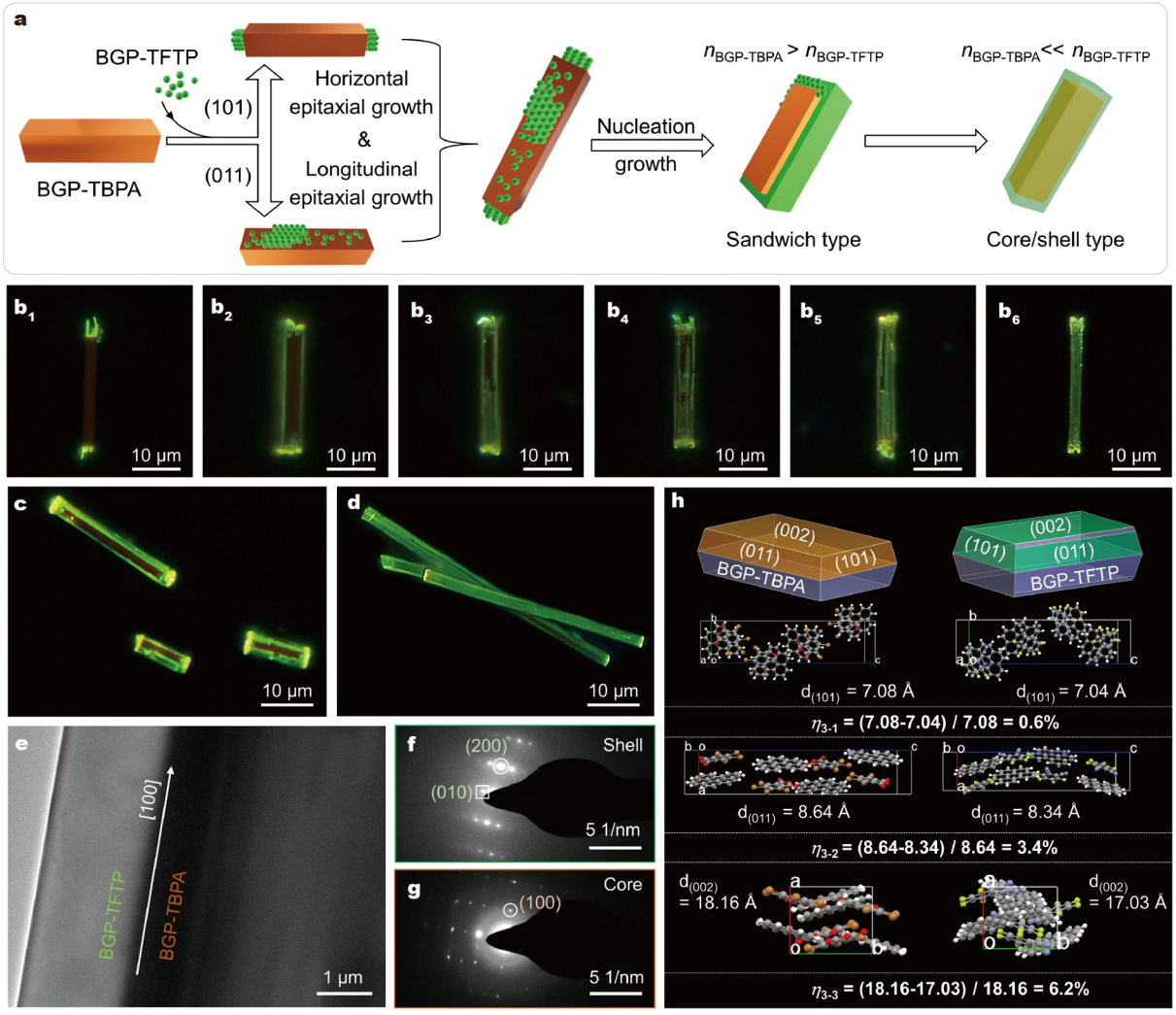

Figure 4 Analysis of sandwich and core/shell heterostructure microwires. (a) Scheme of the selective epitaxial growth of BGP-TFTP microwires on BGP-TBPA microwires to form sandwich and core/shell heterostructures. (b_1–b_6) Evolution processes of core/shell heterostructures from triblock to sandwich to core/shell. (c) FM images of sandwich microwires. (d) FM images of core/shell microwires. (e) TEM image of a typical core/shell microwire. The corresponding SAED patterns of core/shell microwire at (f) edge and (g) central positions. (h) Predicted growth morphology of BGP-TBPA and BGP-TFTP cocrystal, and the corresponding lattice mismatching ratios (η_3) of core/shell heterostructure at three junctions.

of the heterostructure interface clearly shows the continuity of two crystals, which can be ascribed to the good lattice matching between the BGP-TFTP and BGP-TBPA cocrystals (Fig. 4e). The corresponding SAED patterns taken at the core and shell segment of the heterostructure show diffraction spots, which can be ascribed to the (200) and (010) planes of BGP-TFTP and (100) plane of BGP-TBPA (Fig. 4f, g), and demonstrate that the oriented growth of BGP-TFTP and BGP-TBPA both along *a* axis. Moreover, the crystal structure of BGP-TFTP microwires was confirmed by single crystal XRD analysis, and the simulated data demonstrates that the (101), (011) and (002) planes of BGP-TFTP respectively match well with (101), (011) and (002) planes of BGP-TBPA (Fig. 4h). It can be deduced that the epitaxial relationship between the BGP-TFTP cocrystal and the BGP-TBPA cocrystal is $(101)_{BGP-TFTP}||(101)_{BGP-TBPA}$, $(011)_{BGP-TFTP}||(011)_{BGP-TBPA}$ and $(002)_{BGP-TFTP}||(002)_{BGP-TBPA}$. Therefore, it is possible to selectively grow BGP-TFTP on the BGP-TBPA cocrystals, due to the smaller lattice mismatch (η_{3-1} = 0.6%, η_{3-2} = 3.4%, and η_{3-3} = 6.2%). Furthermore, the diffraction peaks belonging to the BGP-TBPA and BGP-TFTP cocrystal can be found in the XRD patterns of heterostructures, indicating the successful synthesis of the heterostructure microwire (Fig. S17). The spatially resolved PL spectra of an individual sandwich microwire (Fig. S18) show that the emission from the edge (location 1) is in good consistence with that of BGP-TFTP. The spectrum from the central (location 2) is dominated by the BGP-TBPA emission, and the emission at the junction includes the emission of two cocrystals, which suggests that the successful synthesis of the desired sandwich heterostructures. Likewise, the structure of the core/shell microwire is confirmed by their spatially resolved PL spectra. The aforementioned results show that compared with the triblock or branch heterostructure, in the sandwich heterostructure, due to the large attachment energy of end planes, the BGP-TFTP microwires priority grow on the end planes of BGP-TBPA along the longitudinal direction (Fig. S16). By using more BGP-TFTP crystal, BGP-TFTP also grow on the edge and basal planes along the horizontal direction to form the core/shell heterostructure, indicating that the

selective epitaxial growth of BGP-TFTP depends on the good lattice matching and attachment energies of the substrate.

Oriented signal conversion based on heterostructures

Organic micro/nanocrystals have been demonstrated as promising building blocks for optical applications due to their good light confinement [40–44]. Herein, we explored the optical waveguide characteristics of cocrystal microwires through micro-area spectroscopy, which was applied to measure the distance-dependent PL spectra. The optical loss coefficients (R) were estimated based on $I_{tip}/I_{body} = A\exp(-RD)$, where D is the propagation distance of photon, A is the ratio of the light escaping from the excitation spot and that of light propagating along the heterostructure, and I_{body} and I_{tip} are the intensities of the body excited site and emitted tip. The resulted R values are 0.0094, 0.0951, 0.0601 and 0.1033 dB μm^{-1} corresponding to BGP-TBPA, BGP-OFN, BGP-TFP and BGP-TFTP cocrystal microwires (Figs S19–S22). As shown in Fig. 5a, the obtained heterostructures with different spatial orientations and interfaces were used as various signal converters and multichannel photon transmission for the construction of integrated photonics based on the active and passive optical waveguides (Fig. S23). In detail, heterostructure microwires with different architectures enable signal conversion and transmission in different directions,

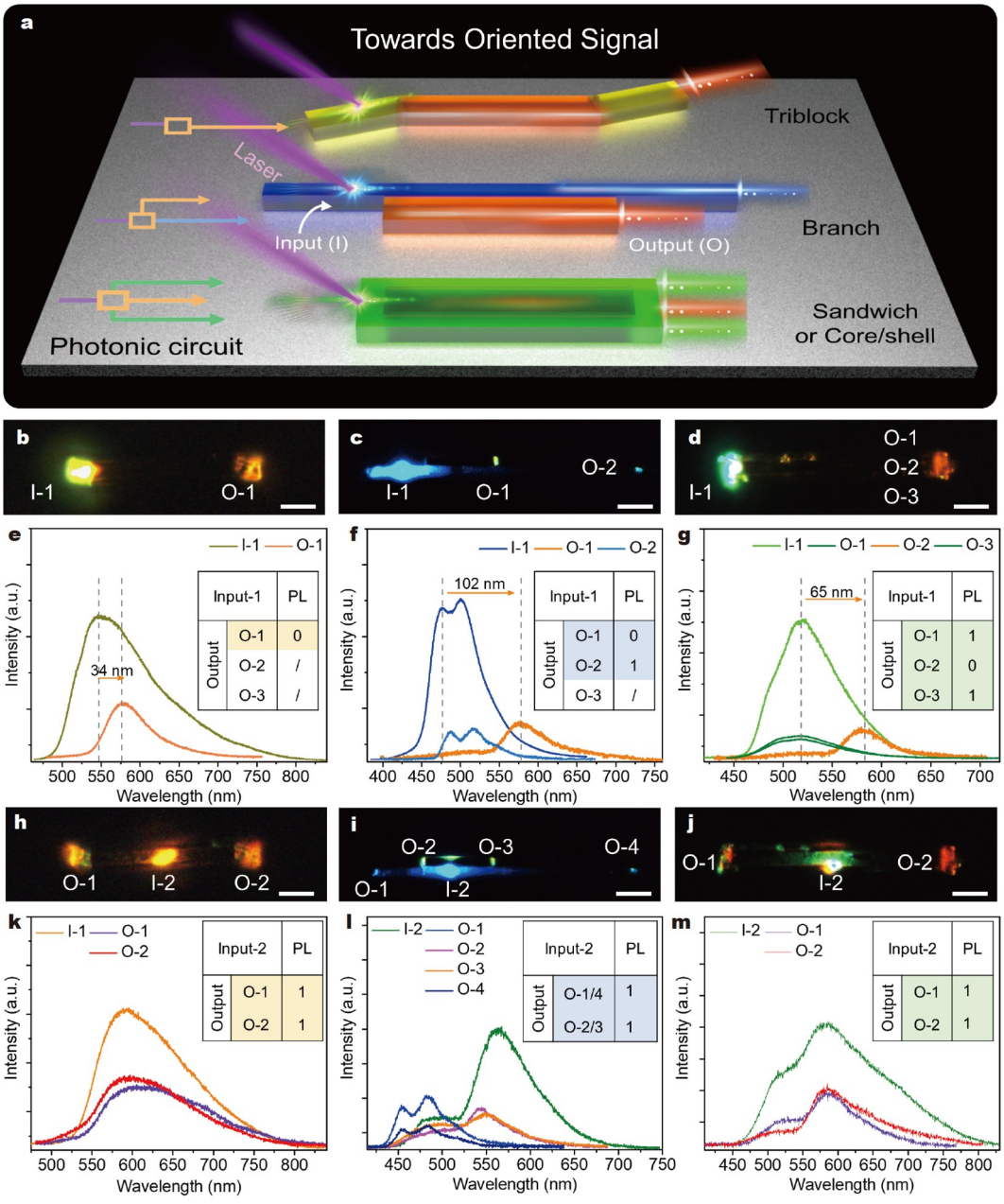

Figure 5 Optical applications of various heterostructured microwires. (a) Organic photonic applications of three types of heterostructures based on active optical waveguides. (b–d) FM images of triblock, branched, and core/shell microwires excited by a laser beam (λ = 375 nm) at Input 1. All scale bars are 10 μm. (e–g) Corresponding spatially resolved PL spectra of different heterostructures excited at Input 1 position. (h–j) FM images of triblock, branched, and core/shell microwires excited by a laser beam (λ = 375 nm) at Input 2. All scale bars are 10 μm. (k–m) Corresponding spatially resolved PL spectra of different heterostructures excited at Input 2 position. The insets are the logic tables that display photon signal output codes.

including single-channel lateral transmission, dual-channel longitudinal transmission, and three-channel transmission combining both lateral and longitudinal directions. Owing to the unique architecture, when the light with 375 nm was introduced at the terminal (labeled I-1) of the heterostructure microwire, the triblock microwire had one output terminal (labeled O-1), the branch microwire had two output terminals (labeled O-1, and O-2), and the sandwich microwire had three output terminals (labeled O-1, O-2, and O-3). When the excitation position moved to the tip part (Input 1) of the triblock microwire, the emission color at another tip (Output 1) was consistent with the BGP-TBPA owing to the active optical waveguide (Fig. 5b, e and Fig. S24). When excited at Input 1 of the branch microwire, because the photon propagation from one tip to the other tips is passive and active waveguide, thus the emission color at Output 1 corresponds to the BGP-TBPA cocrystal while the out-coupled emitting signal Output 2 at 470 and 500 nm corresponds to the emission of the BGP-OFN (Fig. 5c, f and Fig. S25). When excited at the end part (Input 1) of the sandwich microwire, the output light is orange emission, and the spectra of the side both correspond to the BGP-TFTP emission (Fig. 5d, g and Fig. S26) due to the passive propagation of photons, while the spectrum of the central part corresponds to the BGP-TBPA emission based on the active waveguide. When excited at the central portion of the heterostructure microwires, the output light all originates from the corresponding excitation light due to the passive optical waveguide. It is worth noting that the output channels can be divided into one, two, and three categories, which are beneficial to meet different requirements of the optical circuit (Fig. 5h–m). If the output position and the input position have the same emission spectrum, the optical signal is defined as "1", otherwise the signal is defined as "0", and then optical logic circuit tables can be obtained in the insets of Fig. 5. Based on the aforementioned analysis, the excitation position-dependent multicolor emission properties and multi-channel output emission of the heterostructure microwires may be applied in the integrated photonics at the nanoscale.

CONCLUSIONS

In summary, we have reported a strategy of cocrystal engineering for ultralow lattice-mismatch heteroepitaxy of HONs, thus avoiding the structure incompatibilities of distinct components. During the hierarchical self-assembly process, the similar crystal packing and compatibilities of organic cocrystals feasibly enable the low lattice mismatch rate (η), which is crucial for the performance of the final device. By using the BGP-TBPA cocrystal as seeds to hierarchically grow diverse organic crystals, selective epitaxial growth of BGP-based cocrystals on different crystal planes in different directions is realized, leading to the formation of heterostructures including branch, triblock, sandwich, and core/shell microwires. It is worth noting that the ultralow lattice mismatch of heterojunction is dependent on the compatibility of organic cocrystal based on the same donor. Furthermore, we selectively synthesized the substructures of core/shell HONs including triblock and sandwich-like nanowires, thus revealing the role of interfacial energies in modulating the formation of distinctive HONs. As a proof-of-concept application, these obtained HONs demonstrate different photon guidance and manipulation as photonic device prototypes. This strategy paves an avenue to the rational synthesis of heterostructure with low lattice mismatch and opens an insight for understanding of the heterogenous interface formed in such well-defined heterostructures, which could be used for diverse promising applications such as electronics or photonics.

Received 24 May 2023; accepted 21 July 2023; published online 18 September 2023

1 Chen PC, Liu X, Hedrick JL, *et al.* Polyelemental nanoparticle libraries. Science, 2016, 352: 1565–1569
2 Steimle BC, Fenton JL, Schaak RE. Rational construction of a scalable heterostructured nanorod megalibrary. Science, 2020, 367: 418–424
3 Lu Q, Wang AL, Gong Y, *et al.* Crystal phase-based epitaxial growth of hybrid noble metal nanostructures on 4H/fcc Au nanowires. Nat Chem, 2018, 10: 456–461
4 Cortie MB, McDonagh AM. Synthesis and optical properties of hybrid and alloy plasmonic nanoparticles. Chem Rev, 2011, 111: 3713–3735
5 Jiang S, Li L, Wang Z, *et al.* Spin tunnel field-effect transistors based on two-dimensional van der Waals heterostructures. Nat Electron, 2019, 2: 159–163
6 Yang T, Zheng B, Wang Z, *et al.* Van der Waals epitaxial growth and optoelectronics of large-scale WSe_2/SnS_2 vertical bilayer p–n junctions. Nat Commun, 2017, 8: 1906
7 Behura SK, Wang C, Wen Y, *et al.* Graphene-semiconductor heterojunction sheds light on emerging photovoltaics. Nat Photonics, 2019, 13: 312–318
8 Zhang X, Lai Z, Ma Q, *et al.* Novel structured transition metal dichalcogenide nanosheets. Chem Soc Rev, 2018, 47: 3301–3338
9 Wu XJ, Chen J, Tan C, *et al.* Controlled growth of high-density CdS and CdSe nanorod arrays on selective facets of two-dimensional semiconductor nanoplates. Nat Chem, 2016, 8: 470–475
10 Liu J, Niu W, Liu G, *et al.* Selective epitaxial growth of Rh nanorods on 2H/fcc heterophase Au nanosheets to form 1D/2D Rh-Au heterostructures for highly efficient hydrogen evolution. J Am Chem Soc, 2021, 143: 4387–4396
11 Fenton JL, Steimle BC, Schaak RE. Tunable intraparticle frameworks for creating complex heterostructured nanoparticle libraries. Science, 2018, 360: 513–517
12 Miszta K, de Graaf J, Bertoni G, *et al.* Hierarchical self-assembly of suspended branched colloidal nanocrystals into superlattice structures. Nat Mater, 2011, 10: 872–876
13 Tang X, Cui LS, Li HC, *et al.* Highly efficient luminescence from space-confined charge-transfer emitters. Nat Mater, 2020, 19: 1332–1338
14 Lv Q, Wang XD. Low-dimensional organic structures with hierarchical components for advanced photonics. Sci Bull, 2022, 67: 991–994
15 Yu P, Zhen Y, Dong H, *et al.* Crystal engineering of organic optoelectronic materials. Chem, 2019, 5: 2814–2853
16 Wang H, Li Q, Zhang J, *et al.* Visualization and manipulation of solid-state molecular motions in cocrystallization processes. J Am Chem Soc, 2021, 143: 9468–9477
17 Cao J, Liu H, Zhang H. An optical waveguiding organic crystal with phase-dependent elasticity and thermoplasticity over wide temperature ranges. CCS Chem, 2021, 3: 2569–2575
18 Wu JJ, Gao H, Lai R, *et al.* Near-infrared organic single-crystal nanolaser arrays activated by excited-state intramolecular proton transfer. Matter, 2020, 2: 1233–1243
19 Ma S, Du S, Pan G, *et al.* Organic molecular aggregates: From aggregation structure to emission property. Aggregate, 2021, 2: e96
20 Pawlicki M, Collins HA, Denning R , *et al.* Two-photon absorption and the design of two-photon dyes. Angew Chem Int Ed, 2009, 48: 3244–3266
21 Wang H, Liu J, Ye K, *et al.* Positive/negative phototropism: Controllable molecular actuators with different bending behavior. CCS Chem, 2021, 3: 1491–1500
22 Tian QS, Yuan S, Shen WS, *et al.* Multichannel effect of triplet excitons for highly efficient green and red phosphorescent OLEDs. Adv Opt Mater, 2020, 8: 2000556
23 Clark J, Lanzani G. Organic photonics for communications. Nat Photon, 2010, 4: 438–446

24 Zhuo MP, Su Y, Qu YK, *et al.* Hierarchical self-assembly of organic core/multi-shell microwires for trichromatic white-light sources. Adv Mater, 2021, 33: 2102719
25 Zhou Z, Zhao J, Du Y, *et al.* Organic printed core-shell heterostructure arrays: A universal approach to all-color laser display panels. Angew Chem Int Ed, 2020, 59: 11814–11818
26 Ma YX, Chen S, Lin HT, *et al.* Organic low-dimensional crystals undergoing twinning deformation. Sci Bull, 2022, 67: 1632–1635
27 Zhao M, Chen J, Chen B, *et al.* Selective epitaxial growth of oriented hierarchical metal-organic framework heterostructures. J Am Chem Soc, 2020, 142: 8953–8961
28 Lv Q, Wang XD, Yu Y, *et al.* Lattice-mismatch-free growth of organic heterostructure nanowires from cocrystals to alloys. Nat Commun, 2022, 13: 3099
29 Zhang W, Jin W, Fukushima T, *et al.* Supramolecular linear heterojunction composed of graphite-like semiconducting nanotubular segments. Science, 2011, 334: 340–343
30 Yu Y, Zhuo MP, Chen S, *et al.* Molecular- and structural-level organic heterostructures for multicolor photon transportation. J Phys Chem Lett, 2020, 11: 7517–7524
31 Yang C, Gu L, Ma C, *et al.* Controllable co-assembly of organic micro/nano heterostructures from fluorescent and phosphorescent molecules for dual anti-counterfeiting. Mater Horiz, 2019, 6: 984–989
32 Deng X, Yu X, Xiao J, *et al.* Our research progress in heteroaggregation and homoaggregation of organic π-conjugated systems. Aggregate, 2021, 2: e35
33 Luo TJM, MacDonald JC, Palmore GTR. Fabrication of complex crystals using kinetic control, chemical additives, and epitaxial growth. Chem Mater, 2004, 16: 4916–4927
34 Cao M, Zhang C, Cai Z, *et al.* Enhanced photoelectrical response of thermodynamically epitaxial organic crystals at the two-dimensional limit. Nat Commun, 2019, 10: 756
35 Pan M, Zhu YX, Wu K, *et al.* Epitaxial growth of hetero-Ln-MOF hierarchical single crystals for domain- and orientation-controlled multicolor luminescence 3D coding capability. Angew Chem Int Ed, 2017, 56: 14582–14586
36 Tan C, Chen J, Wu XJ, *et al.* Epitaxial growth of hybrid nanostructures. Nat Rev Mater, 2018, 3: 17089
37 Kratzer P, Penev E, Scheffler M. First-principles studies of kinetics in epitaxial growth of III–V semiconductors. Appl Phys A-Mater Sci Processing, 2002, 75: 79–88
38 Liu XT, Wang K, Chang Z, *et al.* Engineering donor-acceptor heterostructure metal-organic framework crystals for photonic logic computation. Angew Chem Int Ed, 2019, 58: 13890–13896
39 Venkatakrishnarao D, Mohiddon MA, Chandrasekhar N, *et al.* Photonic microrods composed of photoswitchable molecules: Erasable heterostructure waveguides for tunable optical modulation. Adv Opt Mater, 2015, 3: 1035–1040
40 Shi YL, Wang XD. 1D organic micro/nanostructures for photonics. Adv Funct Mater, 2021, 31: 2008149
41 Tang B, Tang S, Qu C, *et al.* Side-chain engineering of organic crystals for lasing media with tunable flexibility. CCS Chem, 2022, 1–10
42 Lan L, Li L, Di Q, *et al.* Organic single-crystal actuators and waveguides that operate at low temperatures. Adv Mater, 2022, 34: 2200471
43 Lan L, Li L, Yang X, *et al.* Repair and splicing of centimeter-size organic crystalline optical waveguides. Adv Funct Mater, 2023, 33: 2211760
44 Yang X, Lan L, Li L, *et al.* Remote and precise control over morphology and motion of organic crystals by using magnetic field. Nat Commun, 2022, 13: 2322

Acknowledgements This work was supported by the National Natural Science Foundation of China (52173177 and 21971185), the Natural Science Foundation of Jiangsu Province (BK20221362), and the Science and Technology Support Program of Jiangsu Province (TJ-2022-002). Furthermore, this work was supported by Suzhou Key Laboratory of Functional Nano & Soft Materials, the Collaborative Innovation Center of Suzhou Nano Science & Technology, the 111 Project, the Joint International Research Laboratory of Carbon-Based Functional Materials and Devices, and Soochow University Tang Scholar.

Author contributions Wang XD, Zheng M, and Liao LS proposed the research direction and guided the project. Lv Q synthesized the organic heterostructures, and performed the structural/optical characterizations. Yu YJ and Yu Y performed the TEM measurement and some experiments. Yu Y carried out the EDS measurement. LV Q, Wang XD and Liao LS discussed the interpretation of results and wrote the paper. All authors discussed the results and commented on the manuscript.

Conflict of interest The authors declare that they have no conflict of interest.

Supplementary information Experimental details and supporting data are available in the online version of the paper.

Min Zheng is a full professor at the College of Textile and Clothing Engineering, Soochow University. She received her PhD degree in textile chemistry and dyeing and finishing engineering from Donghua University, China. Her research focuses on the fine synthesis of inorganic and organic nanomaterials and the functional textiles including smart wearable devices and medical antibacterial fibers.

Xue-Dong Wang is a full professor at the Institute of Functional Nano & Soft Materials (FUNSOM), Soochow University. He received his Bachelor's degree in chemistry from Lanzhou University in 2011 and his PhD degree in physical chemistry from the Institute of Chemistry, Chinese Academy of Sciences (ICCAS) in 2016. His research focuses on the fine synthesis of organic micro/nanocrystals and the organic photonics including organic solid-state lasers and optical waveguides.

Liang-Sheng Liao received his PhD degree in physics from Nanjing University, China. After working at Eastman Kodak Company as a senior research scientist from 2000 to 2009, he joined FUNSOM, Soochow University as a full professor. He has over 20 years of research experience on organic optoelectronics. His current research interests include materials and architectures of organic light-emitting diodes, organic solar cells, and perovskite solar cells.

通过共晶工程的选择性外延生长有机异质结构实现光信号定向转换

吕强[1,2], 王雪东[1*], 余悦[1], 俞燕君[1], 郑敏[2*], 廖良生[1,3*]

摘要 分层有机纳米结构(HONs)是一种将具有不同功能的多个成分集成在一个系统中的纳米结构, 其在光电子应用中引起了极大的关注. 然而, 由于不同材料之间结构不相容性的难题, 构建具有超低晶格失配率(η)的HONs仍然面临巨大挑战. 共晶工程提供了探索合理制备HONs的有力手段, 但迄今为止尚未得到系统的证明. 在这里, 我们展示了一种用于HONs的超低晶格失配异质外延的共晶工程策略. 该策略具备足够的通用性, 可实现多种材料的集成从而得到不同空间取向的异质结构. 通过实验合成了一系列典型HONs, 包括三嵌段(η_1 = 0.7%)、分支(η_2 = 0.8%)和核/壳(η_3 = 0.6%)纳米结构, 其晶格失配率远低于先前报道的HONs (5%–10%). 此外, 我们选择性地合成了核/壳的子结构, 包括三嵌段和三明治状纳米线, 揭示了界面能在HONs形成过程中的诱导作用. 作为概念验证, 制备所得的不同异质结构成功实现了光子信号的定向转换, 为构建下一代集成光电器件奠定了坚实的基础.

